

Abstract

Buoyancy fluxes and glacial melt rates at vertical ice-ocean interfaces are commonly parameterized using theories derived for unbounded free plumes. A Large Eddy Simulation is used to analyze the disparate dynamics of free plumes and wall-bounded plumes; the distinctions between the two are supported by recent theoretical and experimental advances and demonstrate that unbounded plume theory does not adequately represent plume/boundary layer dynamics at ice-ocean interfaces. Modifications to parameterizations consistent with these simulations are tested and compared to results from numerical and laboratory experiments of meltwater plumes. These modifications include 50% weaker entrainment and a distinct plume-driven friction velocity in the shear boundary layer up to 8 times greater than the externally-driven friction velocity. Using these modifications leads to 40 times the ambient melt rate predicted by commonly used parameterizations at vertical glaciers faces, which is consistent (and necessary for consistency) with observed melt rates at LeConte Glacier, Alaska.

Plain Language Summary

Over the past two decades, the outward flow of tidewater glaciers has accelerated, which has contributed to sea level rise. There is growing evidence that this acceleration has been triggered by melting at ice-ocean interfaces, where the ocean comes into contact with and drives the melting of glaciers. In particular, commonly used models and theories describing the ocean turbulence and melt dynamics at vertical ice-ocean interfaces underestimate observed melt rates by an order of magnitude. This study tests proposed changes to existing theories and uses a turbulence-resolving ocean model to validate this alternative (plume with a wall) theory instead of commonly used (plume without a wall) theories; the first type better is more appropriate and takes into account how ocean turbulence drives the melting of a vertical ice wall. We show that these proposed changes are consistent with existing melt observations and are an important step towards understanding a critical process that may help us improve sea level rise predictions.

1 Introduction

Outflowing of marine-terminating glaciers at the margins of the Greenland Ice Sheet and Antarctic Ice Sheet has accelerated in recent years (van den Broeke et al., 2016). A major cause of the accelerated melting is postulated to be the warming of deep ocean currents that come into contact with the termini of tidewater glaciers leading to submarine melt (Holland et al., 2008; Straneo & Heimbach, 2013; Wood et al., 2018; Cowton et al., 2018).

At vertical or near-vertical glacier faces, submarine melt is primarily driven by a combination of three dynamical processes: subglacial discharge plumes, ambient melt plumes, and horizontal circulation (Straneo & Cenedese, 2015; Jackson et al., 2019). The first two types of melt are driven by buoyant plume convection of different strengths with vertical velocities reaching 2–3 m/s for subglacial discharge plumes and up to 10 cm/s for melt plumes. The horizontal near-glacier velocity has a magnitude of up to tens of cm/s, varies significantly between fjords and seasons with limited direct observations (Sutherland et al., 2014; Straneo & Cenedese, 2015; Jackson et al., 2019). Although subglacial discharge plumes have the potential to drive the fastest melt rates locally, they are often observed to occupy a small fraction of the glacial face, while the other two melt processes occur across the entire glacial face (Cowton et al., 2015; Slater et al., 2018).

Recent studies have discussed the relative importance of these three melt processes (Slater et al., 2018; Jackson et al., 2019) and most studies using current parameterizations predict ambient melt rates outside of subglacial discharge plumes to be low (much

61 less than a meter/day, often cms per day; Fried et al. (2015); Carroll et al. (2016); Zhao
 62 et al. (2021)). However, there is a mismatch between recent observations and these pa-
 63 rameterizations; measured ambient melt rates are an order of magnitude greater (1-10
 64 meters/day) across the entire submarine terminus, even in parts of the glacier face far
 65 from discharge plumes (Jackson et al., 2019; Sutherland et al., 2019). In addition to the
 66 discrepancy for ambient melt rates, because discharge plumes often cover a small frac-
 67 tion of the total glacier area, the face-averaged and total observed melt rates are also much
 68 higher than those predicted by existing parameterizations.

69 In this study, we extend results from a recently proposed parameterization for verti-
 70 cal glacial ice fronts, which proposed modifying unbounded plume theory using empiri-
 71 cal constraints for the efficiency of turbulent heat and salt transfer to match observa-
 72 tional data (Schulz et al., 2022). Schulz et al. (2022) also proposed a transfer function
 73 that merges the velocity-dependent (shear-dominated) and velocity-independent (buoyancy-
 74 dominated) melt regimes, albeit with a significantly higher buoyancy-dominated melt
 75 rate than previous literature (e.g., Kerr and McConnochie (2015)). In this study, we pro-
 76 pose a physically-motivated melt parameterization that includes both convective- and
 77 shear-dominated melt regimes that is consistent with existing theories, observations, and
 78 laboratory experiments.

79 In section 2, we present an updated and integrated overview of free plumes, wall-
 80 bounded plumes, and horizontal circulation-driven melt, and how each drive the bound-
 81 ary layer dynamics and melt at a vertical ice face. In section 3, we present a set of Large
 82 Eddy Simulations of a subglacial discharge plume with and without a vertical glacier wall
 83 to compare the horizontal and vertical profiles of vertical momentum for unbounded free
 84 plumes and wall-bounded plumes. This is compared with existing theories for discharge
 85 plumes. In section 4, we compare the existing parameterizations of glacial melt rates at
 86 a rapidly melting vertical ice face (LeConte, Alaska) with the updated melt plume the-
 87 ory (section 2) and discharge plume theory (section 3). This shows that wall-bounded
 88 plume theory (after accounting for buoyancy due to melt from horizontal circulation)
 89 is consistent with recent observations, while the commonly used free plume theory un-
 90 derpredicts the melt rate outside of discharge plumes by a factor of 40. Finally, we sum-
 91 marize our key findings and proposed changes to vertical ice-ocean interface parameter-
 92 izations and conclude.

93 **2 Theory of Vertical Ice-Ocean Interfaces**

94 In this section, we summarize and integrate recent developments in vertical ice-ocean
 95 boundary layer parameterizations by first discussing the thermodynamic coupling of the
 96 interfacial boundary layer to the corresponding (plume- or external forcing-driven) outer
 97 velocity, temperature, and salinity. We then discuss how these outer properties are pa-
 98 rameterized for each of the three types of outer boundary layers: subglacial discharge
 99 plumes, ambient face-wide melt plumes, and background/external circulation. We re-
 100 fer the reader to recent reviews of glacial plumes and ice-ocean parameterizations for fur-
 101 ther details and references (Malyarenko et al., 2020; Hewitt, 2020).

102 **2.1 Vertical Ice-Ocean Boundary Layers**

103 Current melt rate parameterizations at vertical ice-ocean interfaces can be classi-
 104 fied into being relevant in either the buoyancy-driven regime (Kerr & McConnochie, 2015)
 105 or the shear-driven regime (McPhee et al., 2008; Jenkins, 2011) based on whether the
 106 rate of turbulent heat flux is primarily driven or constrained by buoyancy flux diffusing
 107 away from the wall (buoyancy-driven) or the momentum flux diffusing towards the wall
 108 (shear-driven); a transition from the first to the second regime occurs if the buoyant up-
 109 draft has gained significant vertical momentum (Wells & Worster, 2008). In the absence
 110 of externally-forced circulation or turbulence, vertical ice-ocean interfaces start off as wholly

111 laminar boundary layers within the first 10–30 cm above their initiation point before they
 112 transition to the buoyancy-driven turbulent regime (Josberger & Martin, 1981; Wells &
 113 Worster, 2008); however, we do not discuss the laminar regime further due to its lim-
 114 ited relevance to the geophysical scale of glaciers.

Within buoyancy-driven boundary layers, the melt rate is velocity-independent and can be approximated as (Kerr & McConnochie, 2015)

$$m_B = 0.25(T - T_f(S))^{4/3}, \text{ for } Ra < R_c \quad (1)$$

(in $\mu\text{m } ^\circ\text{C}^{-4/3} \text{ s}^{-1}$) where T is the ambient temperature, T_f is the local freezing temperature (which can be calculated using the liquidus condition similarly to SI Eq. (7c)) at ambient salinity S . For shear boundary layers,

$$m_S = c_w \gamma_T (T - T_b) \hat{L}^{-1}, \text{ for } Ra > R_c, \quad (2)$$

115 and $\hat{L} \equiv L + c_i(T_b - T_i)$. Here, $c_w = 3974 \text{ J kg}^{-1}\text{ }^\circ\text{C}^{-1}$ and $c_i = 2009 \text{ J kg}^{-1}\text{ }^\circ\text{C}^{-1}$ are the
 116 specific heat capacity of water and ice, respectively, $L = 3.35 \times 10^5 \text{ J/kg}$ is the latent
 117 heat of ice, γ_T is the turbulent thermal transfer coefficient (with units of velocity), and
 118 T_b is the boundary layer temperature predicted by solving the 3-equation thermodynam-
 119 ical balance (see SI S-1). In the case of LeConte glacier, which is abutted by warm fjord
 120 waters (up to $8 \text{ }^\circ\text{C}$), T_i is nearly $0 \text{ }^\circ\text{C}$. The turbulent transfer coefficient is dependent
 121 on the friction velocity and is discussed in the next subsection.

Here, the threshold between buoyancy-driven and shear-driven boundary layers is set by a critical value of the buoyancy Rayleigh number $Ra = b(z - z_0)^3 / (\nu\kappa)$, which represents the plume’s increasing convective efficiency with respect to diffusion with height from the source ($z - z_0$), where $\nu = 1.8 \times 10^{-6} \text{ m}^2/\text{s}$ is the viscosity and $\kappa = 7.2 \times 10^{-10} \text{ m}^2/\text{s}$ the salt diffusivity of seawater. The critical Rayleigh number Ra_c for the transition and its corresponding transition height $z_c - z_0$ is the subject of some debate (Grossmann & Lohse, 2000; Wells & Worster, 2008), partly due to the fact that this transition has not been observed in a natural setting, but it is postulated to occur at $Ra_c = 10^{21}$ (Kerr & McConnochie, 2015). Recent laboratory experiments suggest that this occurs at a vertical velocity of 0.03 to 0.05 m/s for a discharge plume at $3.5 \text{ }^\circ\text{C}$ above freezing (McConnochie & Kerr, 2017a). A simple way to combine the two regimes in Eqs. (1) and (2) is to use a melt rate prediction based on the dominant turbulent transfer process at the boundary layer, resulting in

$$m = \max\{m_S, m_B\}. \quad (3)$$

122 2.2 Shear-Driven Turbulent Transfer

The turbulent transfer coefficient in a shear-dominated regime is commonly expressed in terms of horizontal (v) and vertical (w) near-glacier ocean velocities as

$$\gamma_T = \underbrace{\sqrt{C_d \Gamma_T}}_{St} \sqrt{v^2 + w^2}, \quad (4)$$

123 with a drag coefficient C_d ranging from 0.001 to 0.0097. See Fig. 1a for a schematic of
 124 the different boundary layers and corresponding velocities. In the absence of boundary
 125 layer observations, a commonly used placeholder value of $C_d = 0.0025$ is used in the
 126 ice plume literature along with a turbulent heat transfer constant $\Gamma_T = 0.022$ (Jenkins
 127 et al., 2010). However, this does not distinguish between the frictional boundary layer
 128 thickness (via C_d) in the horizontal and vertical and more important, it does not dis-
 129 tinguish between the external velocity-field driven shear boundary layers and the plume-
 130 driven boundary layers. For melt plumes and discharge plumes, it is also unclear how
 131 v and w should be defined as both far-field velocities for plumes are zero.

The total shear stress at a shear boundary layer is the sum of both the viscous and turbulent shear stresses

$$\frac{\tau}{\rho} = \underbrace{\nu \partial_x \bar{w}}_{\text{viscous stress}} - \underbrace{\overline{u'w'}}_{\text{Reynolds stress}}. \quad (5)$$

132 In most externally-forced wall-bounded shear flows (in either the atmospheric bound-
 133 ary layer or horizontal ice-ocean boundary layers; Jenkins (1991); Kaimal and Finnigan
 134 (1994); Pope (2000)), the turbulent Reynolds stress dominates the momentum dissipa-
 135 tion contribution. However, recent laboratory and numerical experiments suggest that
 136 plume-driven buoyancy forcing at an ice-ocean interface behaves differently than the ex-
 137 ternal far field-forced velocity field. This is because buoyancy (from melting) is gener-
 138 ated directly at the interface itself in melt plumes or close to the wall in the case of sub-
 139 glacial discharge plumes (Gayen et al., 2016; Parker et al., 2020, 2021). Therefore, it is
 140 important to distinguish shear stresses associated with the external velocity field from
 141 those of the internal plume-driven shear stresses. For both melt plumes and discharge
 142 plumes, more of the shear stress contribution is viscous in Eq. (5) and thus, more of the
 143 kinetic energy is dissipated before becoming turbulent.

However, this has been demonstrated to lead to a melt rate that scales strongly with
 the friction velocity of the shear boundary layer (Gayen et al. (2016); McConnochie and
 Kerr (2017b); Parker et al. (2020, 2021)). In order to separate the individual contribu-
 tions of plume-driven shear and externally-driven shear, we express the turbulent ther-
 mal transfer coefficient (and similarly for the turbulent salinity transfer coefficient) as

$$\gamma_T = \Gamma_T (v_*^2 + w_*^2), \quad (6)$$

144 where the plume-driven friction velocity is defined such that $w_*^2 = \nu \partial_x \bar{w}_p|_{x=0}$ at a ver-
 145 tical wall $x = 0$, for a time-averaged plume vertical velocity w_p (which assumes all of
 146 the viscous stress is converted to turbulent stress). Eq. (6) is a simple way of combin-
 147 ing the horizontal and vertical components friction velocity via the velocity magnitude,
 148 which is commonly used when there is a 2D external velocity field (Jenkins, 2011), but
 149 such an expression has not been validated for combining plume-driven friction velocity
 150 and externally-driven friction velocity (see McConnochie and Kerr (2017b) for further
 151 discussion).

152 In previous studies, the plume-driven shear boundary layer is often expressed using
 153 an equivalent skin friction coefficient $C_d^p \equiv w_*^2/W_p^2$ with empirically derived esti-
 154 mates that are significantly higher than its analogously-defined externally-forced coun-
 155 terpart $C_d^e \equiv v_*^2/v_\infty^2$ for a far-field velocity v_∞ ($C_d^{\text{ext}} \approx 0.0025$, whereas $C_d^p \approx 0.015$
 156 for discharge plumes, and $C_d^p \approx 0.15$ for melt plumes; Gayen et al. (2016); Parker et
 157 al. (2020, 2021)). The characteristic plume velocity W_p used in this parameterization is
 158 defined as the horizontally-integrated mass flux divided by momentum flux (see suppl-
 159 emental material S-1.2 for further discussion).

160 2.3 Theory of Unbounded Free Plumes

161 We first discuss buoyant plume convection in the absence of a wall, which is an ex-
 162 tensively studied subject (Morton et al., 1956; Turner, 1979). A 1D theory for the ver-
 163 tical (along-plume) variation in characteristic vertical velocity $W(z) = W_p(z)$, buoy-
 164 ancancy $B(z)$, and plume width $D(z)$ can be solved using the Boussinesq conservation laws
 165 of mass, momentum, and buoyancy, and empirically-derived entrainment assumption (see
 166 SI S-1 for further details). Here, $W(z)$ and $B(z)$ are defined as the mean of the verti-
 167 cal velocity w_p and buoyancy $b = -g(\rho - \rho_a)/\rho_0$ over the plume width for a plume den-
 168 sity ρ , an ambient density ρ_a , and reference density ρ_0 . This theory relies on the empirically-
 169 supported assumption originating from Morton et al. (1956), that the local time-mean
 170 entrainment at each depth is proportional to the characteristic vertical velocity $W(z) =$
 171 $-\alpha U(z)$ for a horizontal inflow velocity magnitude $U(z)$ and constant entrainment co-
 172 efficient α .

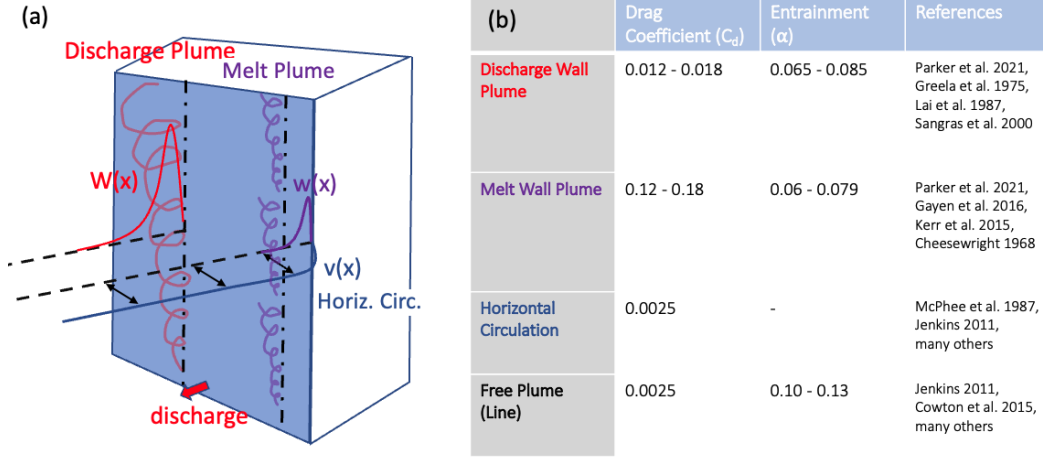


Figure 1. (a) An overview schematic of wall-bounded discharge and melt plume and the ice-ocean boundary layer. The horizontal and vertical velocity profiles for the discharge plume and melt plume ($v(x)$, $W(x)$, and $w(x)$, respectively) are illustrative and not to scale. (b) A table of reference ranges of drag coefficient C_d and plume entrainment coefficient α corresponding to the three types of ice-ocean boundary layers compared to the commonly-used free plume parameterization and their references.

For plumes at an ice-ocean interface, this has been modified to include an accounting of the heat budget, which is a necessary component in calculating the melt rate in Eq. (1) or (2). Therefore, we have the following commonly-used system of equations for 1D line plume evolution originating from Jenkins (1991)

$$\frac{\partial(DW)}{\partial z} = \alpha W + m, \quad (7a)$$

$$\frac{\partial(DW^2)}{\partial z} = DB - C_d^p W^2, \quad (7b)$$

$$\frac{\partial(DWT)}{\partial z} = \alpha WT_a + mT_{ef}, \quad (7c)$$

$$\frac{\partial(DWS)}{\partial z} = \alpha WS_a + mS_i. \quad (7d)$$

173 where m is the melt rate, S_i is the ice salinity and each of the parenthetical terms are
 174 integrated numerically in z to generate the 1D plume solution (see SI S-1 for a deriva-
 175 tion). Note that m and the effective thermal gradient T_{ef} (i.e., the boundary layer tem-
 176 perature and salinity) must be calculated using 3-equation thermodynamics (see SI S-
 177 1). This 1D plume theory has been used extensively in the parameterizations of verti-
 178 cal ice faces (Jenkins, 2011; Cowton et al., 2015; Slater et al., 2018; Jackson et al., 2017,
 179 2019; Sutherland et al., 2019; Zhao et al., 2021) due to its simplicity.

180 Note that this system of equations is valid for both discharge plumes (for an ap-
 181 propriate initial mass and momentum) and melt plumes (for approximately zero initial
 182 mass and momentum). These equations can be modified slightly to describe a point source
 183 (by replacing plume width D with plume radius R and deriving the appropriate conser-
 184 vation laws for a radial symmetry). However, line discharge plumes (a finite width buoy-
 185 ancy source instead of a point source) have been shown to better reproduce existing near
 186 glacier melt fraction observations, but this may be more attributed to the source width
 187 parameter instead of the dynamics (Jackson et al., 2017).

For comparison with wall-bounded plume profiles discussed in the next subsection, the commonly used velocity profile $w(x)$ for free plumes has been determined experimentally and is well-characterized by a Gaussian curve (Ramaprian (1989), Paillat and Kaminiski (2014); suggestive of a random walk of water mass parcels)

$$w(\hat{x}) = W_{\max}(z) \exp\left(\frac{-\hat{x}^2}{D^2}\right), \quad (8)$$

188 where $\hat{x} = x/(z-z_0)$ is the z -scaled x coordinate (such that the plume profiles $w(\hat{x})/W_{\max}(z)$
 189 collapse to a single characteristic profile by similarity with height from the source, $z-$
 190 z_0) and the maximum plume velocity at the plume centerline $W_{\max} \approx 1.35W$.

191 Although the line plume theory momentum flux equation in Eq. (7b) from Jenkins
 192 (1991) includes a skin friction term at the wall, C_d^p has a confusing interpretation if a
 193 wall does not exist as its value depends on the wall-bounded shear boundary layer ver-
 194 tical velocity profile and the boundary layer width. This term owes its commonly used
 195 value of 0.0025 in ice-ocean applications largely to observations at weakly melting nearly
 196 horizontal ice-ocean interfaces (McPhee et al., 1987; Jenkins et al., 2010), which have
 197 boundary layers that can be well-approximated by Monin-Obukhov theory (Vreugdenhil
 198 & Taylor, 2019); this value of skin friction is also commonly used in most other passive
 199 surfaces.

200 2.4 Theory of Wall-Bounded Plumes

201 In the presence of a vertical wall, the 1D line plume theory in Eqs. (7a)–(7d) still
 202 holds with a drag coefficient C_d^p that can now be diagnosed experimentally or numer-
 203 ically via the balance of bulk momentum balance terms in Eq. (7b). In a wall-bounded
 204 plume with a shear layer, the across-plume gradients determined experimentally and nu-
 205 merically differ greatly from the Gaussian-shaped vertical momentum profiles of free plumes
 206 and as a result, different distributions of horizontal turbulent fluxes of momentum and
 207 buoyancy (Sangras et al., 2000; Parker et al., 2020, 2021).

208 These disparities are owed to two major differences between a plume convecting
 209 along a wall vs. one without a wall: the impermeability condition (u at the wall is zero)
 210 and the no-slip condition (w at the wall is zero). Experiments have shown that the im-
 211 permeability condition leads to reduced eddy meandering and weaker mixing of buoy-
 212 ant fluid away from the wall. This produces higher near-wall vertical momentum, which
 213 together with the no-slip condition contribute to significantly higher shear stresses (Parker
 214 et al., 2020, 2021). For discharge plumes, the shear stress diagnosed from laboratory and
 215 numerical experiments exerts a drag on momentum equivalent to 15% of the buoyancy
 216 force for discharge plumes (Parker et al., 2020) and 65% of the buoyancy force for melt
 217 plumes in small (1 meter tall), unstratified domain heights (Gayen et al., 2016; Parker
 218 et al., 2021). These experimentally-derived estimates imply a drag coefficient of $C_d^p =$
 219 0.015 for discharge plumes, and $C_d^p = 0.15$ for melt plumes along with significantly lower
 220 entrainment: $\alpha = 0.075$ for discharge plumes, and $\alpha = 0.068$ for melt plumes. See Fig.
 221 1b for a list of the drag coefficients, entrainment, and a corresponding list of references.

A significant body of experimental and theoretical work supports an across-plume
 vertical velocity profile in the heated wall (free convection literature), which was first ap-
 proximated in Eckert and Jackson (1950) as

$$w(\hat{x}) = W_{\max} \hat{x}^{1/7} (1 - \hat{x})^4. \quad (9)$$

222 This velocity profile also approximately matches recent experiments of ice-ocean bound-
 223 ary layers (Parker et al., 2021). However, it is unknown how these dynamics play out
 224 at much larger Ra and rise heights in the well-developed shear boundary layers (Eq. (2))
 225 due to complications of a much weaker solutal diffusivity (where the Schmidt number
 226 $Sc = \nu/\kappa_S \approx 2600$ for seawater), although in theory it is analogous to the large Prandtl
 227 $Pr = \nu/\kappa_T$ regime.

2.5 Horizontal Circulation-Driven Melt

The near-glacier horizontal velocity has a very different profile $v(x)$ compared to the across-plume vertical velocity profile $w(x)$ (see Fig. 1a), where the commonly used parameterization uses the far-field background velocity $v(\infty)$ (at 10-100 m away from the boundary) and a drag coefficient of $C_d^{\text{ext}} = 0.0025$ (consistent with a meter scale law-of-the-wall log layer). By comparison, plume-driven shear boundary layers are much thinner (centimeters or less) and they have proportionally larger friction velocities compared to the outer velocity ($C_d^{\text{ext}} = v_*^2/v_\infty^2 \ll C_d^{\text{p}} = w_*^2/W_p^2$).

The far-field velocity $v(\infty)$ may either be observed directly (estimated to be 20 cm/s near the face of LeConte (Jackson et al., 2019)) or parameterized using the theory from Zhao et al. (2021, 2022), which uses a steady state balance between vorticity supplied by the discharge and melt plumes and bottom drag for a given density layer bounded by $z = z_\rho$ and $z_{\rho'}$ as

$$v_n(\infty) \approx \frac{2f\psi}{C_F C_d^{\text{ext}}(z_{\rho'} - z_\rho)}. \quad (10)$$

Here ψ is the near-glacier overturning strength (which can be calculated using the plume theory for W and using the entrainment assumption $\partial W(z) = -\alpha U(z)$; see Sections 2.2 and 2.3)

$$\psi = \max_{z'} \int_0^{W_f} \int_{z_{\rho'}}^{z_\rho} U \, dz' \, dy', \quad (11)$$

for Coriolis parameter f , fjord width W_f , and the fjord perimeter at the depth of a given density layer C_F . See Zhao et al. (2021, 2022, 2023) for additional details.

3 Large Eddy Simulations of Subglacial Discharge Plumes

Although recent experimental and numerical studies (discussed in Section 2.3, Gayen et al. (2016); Parker et al. (2020, 2021)) demonstrated a larger wall shear stress and weaker entrainment in wall-bounded discharge plumes compared to free plumes, those experiments were not able to diagnose the relative importance of the two wall effects: impermeability and the no-slip boundary condition. In the following experiments, we test the importance of these two effects separately. We examine the horizontal profiles and vertical acceleration of vertical velocity to reconcile the differences (particularly how it is treated in the glacial context) between the theory of unbounded free plumes and wall-bounded plumes.

3.1 Model Setup

To examine the difference between a wall-bounded plume and a free plume, we conduct a series of Large Eddy Simulations (LES) of an idealized near-glacier fjord domain using the Massachusetts Institute of Technology general circulation model (MITgcm; Marshall et al. (1997)). The vertical and horizontal resolution are both 1 m and we use a 3D Smagorinsky viscosity parameterization with a coefficient of 0.03 (Smagorinsky, 1963). The model is forced on the open-ocean side by an idealized temperature/salinity (Fig. 2b) based on August 2016 observations at LeConte Glacier, Alaska (Jackson et al., 2019). For the cases with a vertical wall, we parameterized melting at the ice face using a shear boundary layer assumption and 3-equation thermodynamics (Eqs. (2) and (4)). This differs from many previous studies, which often assume a fixed buoyancy flux with depth (Parker et al., 2020, 2021). We use an idealized bathtub domain with smooth sidewalls (see Fig. 2a for the bathymetric variation in y) for a 200m deep, 1 km wide (in y) by 2 km long (in x) fjord section with a subglacial discharge of 150 m³/s, which is distributed at the $x = 1$ m boundary as a source of mass inflow. To help initiate turbulent motions near the source, the mass source is distributed at 10 evenly-spaced outlets over a 100 meter extent in y ($450 \leq y \leq 550$ m) at $z = -200$ m, which provides a small degree of along- y asym-

275 metry in vertical momentum without any meaningful influence on the y -integrated ver-
 276 tical momentum. The length of this fjord section minimizes the interaction between the
 277 plume-generated turbulence and the open ocean boundary at $x = 2000$ m. See SI S-2
 278 for additional details of the numerical model.

279 3.2 Simulation Results

280 Fig. 2a, c, d show the near-face ($x=3$) vertical velocity, $w = 0.2$ m/s velocity sur-
 281 face, and meridionally-averaged vertical velocity for a reference case of a wall-bounded
 282 discharge plume at an ice-ocean boundary without drag. This shows the development
 283 of 3D convective turbulence, which develops due to xz -plane vorticity sourced at $y =$
 284 450, 550 m on the margins of the line plume and throughout the plume due to vortic-
 285 ity aligned in the yz -plane; these regions correspond to high horizontal shear in verti-
 286 cal velocity leading to turbulent shear production. Although a finer grid would better
 287 resolve the smaller scales of turbulence at depths especially near the plume source, the
 288 turbulence in the upper half of the plume is sufficiently well-developed to calculate across-
 289 plume profiles of vertical velocity. Fig. 2d also shows the mean meridionally-averaged
 290 density field, whose positive buoyancy anomaly within the plume is the source of the buoy-
 291 ancy flux driving upward acceleration. This also shows the gradual decrease in density
 292 along the plume due primarily to the entrainment of ambient water.

293 To compare the characteristics of free plumes and wall-bounded plumes, we exam-
 294 ine three test cases. The first case is a free plume, the second case is a wall plume with-
 295 out drag at the wall, and the third case is a wall plume with a drag coefficient of $C_d =$
 296 0.015 to emulate the no-slip condition (which is parameterized and not resolved). Note
 297 that this value of drag coefficient is determined for discharge plumes (which is distinctly
 298 lower than than the effective drag felt by a melt plume) and is obtained experimentally
 299 (see Section 2b and Fig. 1b).

300 Fig. 3a shows the horizontal variation of vertical velocity $w(x)$ and Fig. 3b shows
 301 the vertical variation of characteristic vertical velocity $W(z)$ for each of the three test
 302 cases. These demonstrate that the dynamics are consistent with their respective theo-
 303 ries; free plumes $w(x)$ are well approximated by the Gaussian profiles in Eq. (6) and wall-
 304 plume profiles are consistent with the turbulent wall-plume theory in Eq. (7). These func-
 305 tions were fit using α as a free parameter (which determines the characteristic width scale
 306 D of the plume for a given $z - z_0$). For the free plume case, this implies $\alpha = 0.14$; for
 307 the wall-plume case without drag, $\alpha = 0.083$; for the wall-plume case with drag, $\alpha =$
 308 0.079. These diagnosed values are consistent with those from previous studies (Fig. 1b).

309 Fig. 3b shows the vertical variation of the characteristic vertical velocity $W(z)$ along
 310 with the corresponding theoretical solutions from 1D plume theory (Eq. (5)). This com-
 311 parison demonstrates that the bulk mean vertical momentum W is consistently well-predicted
 312 by plume theory in these simulations. In particular, 1D plume theory captures the 17%
 313 increase in W for the wall-bounded free plume and the smaller 6% increase in W when
 314 drag is added (due to the additional buoyancy flux from melt). Note that the charac-
 315 teristic width of the wall-bounded plume is much narrower (in Fig. 3a), partially due to
 316 weaker entrainment for the wall-bounded plumes and not as much acceleration of the
 317 characteristic vertical velocity, which is consistent with 1D plume theory. A notable caveat
 318 here is that near the source of the plume, the plume is not fully resolved at the 1 m hor-
 319 izontal resolution used in these simulations and likely contributes to the small mismatch
 320 in vertical momentum there. Near the depth of neutral buoyancy at the top of the plume,
 321 there is also a similar discrepancy between the theory and simulations, but this is likely
 322 caused by additional sources of mixing/instabilities not captured by the theory at these
 323 depths.

324 In summary, these results show that the presence of a vertical wall strongly alters
 325 the dynamics. However, we demonstrate that existing parameterizations (based on the-

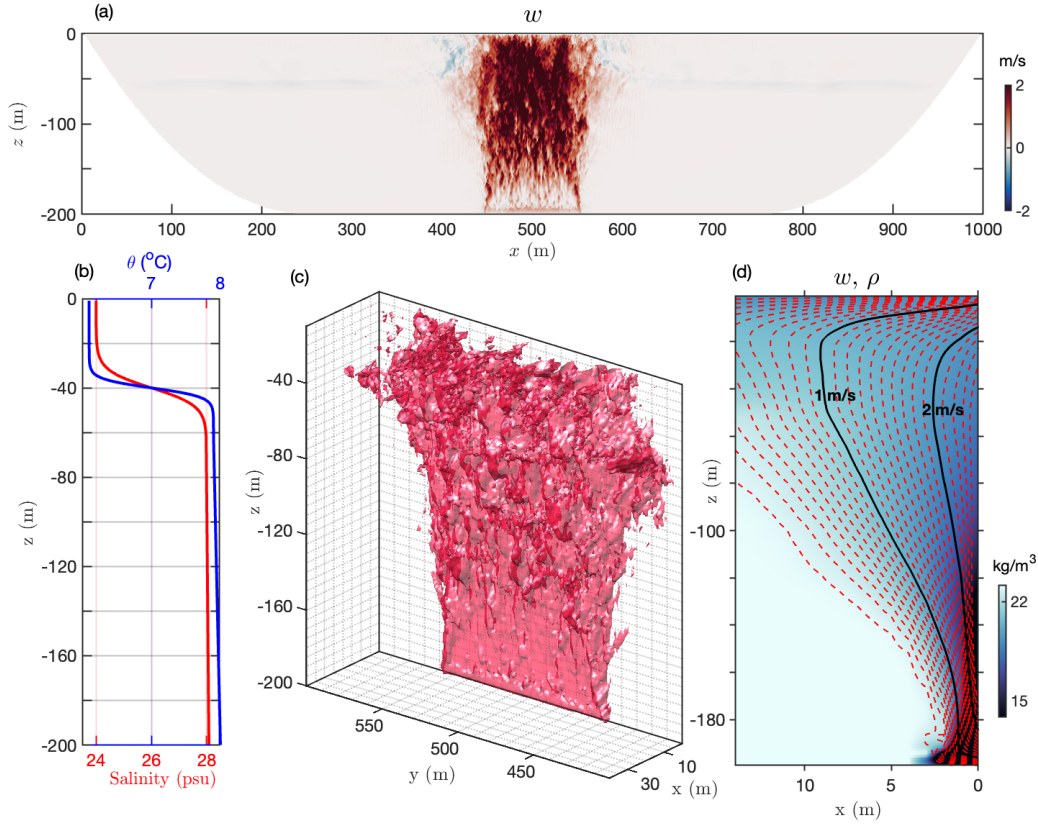


Figure 2. (a) Vertical velocity w (m/s) at $x = 3$ m away from the ice. (b) Open-ocean boundary condition profiles of conservative temperature θ_a and salinity S_a . (c) The vertical velocity surface $w = 0.2$ m/s. (d) Meridionally-averaged vertical velocity contours from 0.0 to 2.3 m/s (orange is 0.1 m/s spacing, black is 1.0 m/s spacing) plotted on density (in color).

326 ory for unbounded/free plumes), can be adapted to produce the observed variability if
 327 a lower entrainment coefficient is used. In addition, the critical difference between the
 328 entrainment of free and wall-bounded plumes emerges primarily due to the impermeabil-
 329 ity condition and to a lesser extent, the no-slip condition, although the latter is implicit
 330 in the shear boundary layer parameterization (just not as important for the vertical mo-
 331 mentum balance). One caveat of these experiments is that the near-wall horizontal res-
 332 olution in these LES does not allow the near-glacier plume-driven boundary layer to be
 333 fully resolved, which appears to be much more important in melt plumes where the wall
 334 shear stress decreases the total plume momentum by approx. 65% in both laboratory exper-
 335 iments and Direct Numerical Simulations (DNS) (Parker et al., 2021; Gayen et al.,
 336 2016). The resolution and computational cost required to resolve the laminar boundary
 337 layer (in e.g., Gayen et al. (2016)) would not currently be affordable at vertical scales
 338 larger than a few meters. Therefore, we cannot simultaneously simulate the large-scale
 339 discharge plume dynamics while resolving the dynamics of the melt plumes and viscous/diffusive
 340 boundary layers. Instead, the drag coefficient and entrainment rates from small-scale lab-
 341 oratory experiments and DNS (Parker et al., 2021; Gayen et al., 2016) are used to sup-
 342 plement the melt parameterization for melt plume-driven boundary layers in the follow-
 343 ing section.

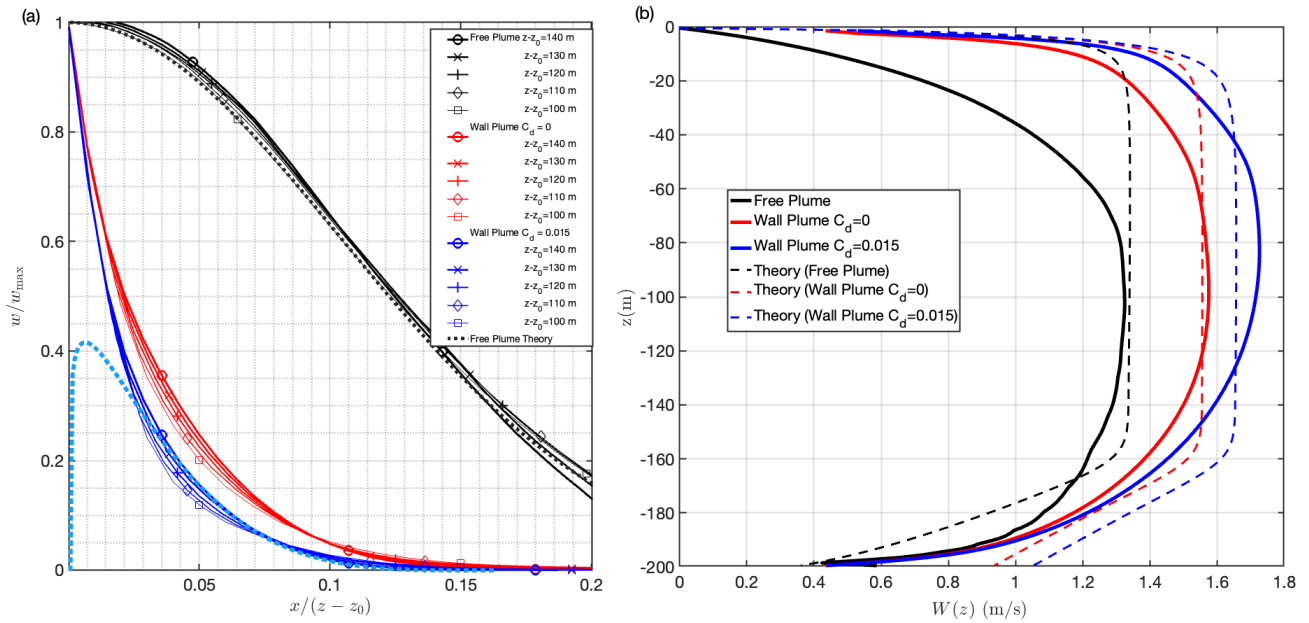


Figure 3. (a) The horizontal variation of vertical velocity $w(x)$ for three test cases: free plume (black), wall-bounded plume without wall drag (red), and wall-bounded plume with wall drag (blue) with theoretical predictions based on Eqs. (8)–(9) for the free plume, and wall-bounded plume with drag case. (b) The vertical variation of characteristic vertical velocity $W(z)$ for each of the three cases in (a) with plume-theory solutions using Eq. (7a)-(7c).

4 Application of Theory to Observations at LeConte Glacier, Alaska

In this section, we apply the synthesized melt and plume theories discussed in Section 2 to observations at a rapidly melting vertical ice face. This is motivated by recent estimates of glacial melt rate using repeat multibeam measurements at LeConte Glacier, Alaska (Sutherland et al., 2019), which observed much larger melt rate estimates than those predicted by prior applications of melt plume theory (Jackson et al., 2019).

Fig. 4 shows a comparison between the melt rate and plume velocity at LeConte Glacier using the temperature and salinity profiles from the August 2016 field campaign (panel c, Sutherland et al. (2019)). This demonstrates a significant difference in melt rate distribution at LeConte glacier calculated using the traditional free plume melt parameterization (panel (a)) vs. the updated wall plume melt parameterization (panel (b)). In particular, the free plume melt parameterizations uses the different representation of the turbulent transfer coefficient in Eq. (4) vs. the updated from Eq. (6), with horizontal melt included (assuming a uniform horizontal velocity of 0.2 m/s). For the updated wall plume melt parameterization (panel (b)), we also use a smaller entrainment coefficient α and much larger $C_d^P = 0.15$ consistent with wall-bounded melt plumes, and the horizontal velocity (which influences the melt rate directly in Eq. (3), but also the 1D plume theory in Eq. (7)). Including these differences results in a maximum melt rate that increases from <0.1 m/day to 2.2 m/day and much larger separation distance between meltwater intrusions (the darker colors in these panels show where plumes intrude/new plumes form; see Jackson et al. (2019) for a discussion of these intrusions). See Fig. S1 in the SI for additional panels that reflect the melt rates for the free plume theory with horizontal circulation and discharge plume scenarios.

The characteristic vertical velocity is shown in panel (d) for 4 different cases: a free plume (with low drag and high entrainment), a free plume with horizontal circulation-driven melt, a wall plume without horizontal circulation, and a wall plume with horizontal circulation. This shows that the including horizontal velocity-driven melt for a free plume and using wall-bounded plume (drag and entrainment) coefficients have similar effects; they increase the vertical velocities from less than 0.01 m/s to 0.04 m/s and also increase the intrusion separation distance by a factor of 5. If a horizontal velocity-driven melt is included for a wall-bounded plume, their combined effects compound for weakly stratified depths (e.g., $z = -170$ to -90), while they do not differ from their component effects for strong stratified depths (e.g., $z = -80$ to -40) since the increased inertia is still not adequate to overcome the background stratification. Note that the wall-bounded plumes and horizontal circulation cases produce reasonable intrusion separation distances comparable to the observations from Jackson et al. (2019) while the free plume coefficients does not.

In panel (e), the meridionally-averaged melt rates from panel (c) is compared with a discharge plume added (black), the melt rate estimates from the repeat multibeam survey, and the buoyancy-controlled melt rate using Eq. (1). The melt rate estimate for buoyancy-controlled boundary layers is shown for comparison (approx. 0.3 m/day using Eq. (1)). For melt plumes, this leads to an overall effect of amplifying melt rates at all depths by a factor of 40, which can be attributed to 8x due to increased C_d^P compounded with 5x from the horizontal circulation-driven melt. The horizontal circulation component contributes directly to the melt and buoyancy input (via Eq. (4)), which feeds back on the melt plume's vertical velocity (via Eq. (5)). In the discharge plume case, the buoyancy flux increase is relatively minor ($< 2\%$ since the buoyancy flux from melting is very small compared to the buoyancy flux from the discharge plume), so there is no feedback between the additional melting and vertical momentum of the plume. These higher melt rates leads to proportional higher buoyancy fluxes and overturning circulation within the fjord.

395 In summary, the total, local melt rates, and meltwater intrusion depths are con-
 396 sistent between the observations and the updated wall plume theory when horizontal cir-
 397 culation is included, while the melt is significantly underpredicted by using free plume
 398 theory alone. The melt rates are somewhat underpredicted by using wall-plume theory
 399 without horizontal circulation or free plume theory with horizontal circulation.

400 5 Summary and Conclusions

401 In this study, we provide evidence to support the claim that wall-bounded plumes
 402 very different dynamically from free plumes. We propose an updated parameterization
 403 that uses physically-reasonable values for the turbulent transfer coefficients, melt rates,
 404 and entrainment for wall bounded plumes and vertical ice-ocean interfaces. We then test
 405 the impact and validate (using large eddy simulations and observations) these updated
 406 parameterizations.

407 These differences are summarized as follows: (1) The plume-driven drag coefficient
 408 (C_d^p) is distinct from the externally forced drag coefficient (C_d^{ext}). Unlike an unstrati-
 409 fied flow over a flat plate, C_d^p is not a drag coefficient in the classical sense as it does not
 410 depend on the roughness of the surface: in these theories it is used as a means of quan-
 411 tifying the buoyancy-driven turbulence and momentum budget. As such, it is necessary
 412 to a drag coefficient that is relevant to the dynamics in question. Based on recent nu-
 413 merical and laboratory experiments, estimates of the plume-driven drag coefficients have
 414 been proposed for discharge plumes ($C_d^p = 0.015$) and melt plumes ($C_d^p = 0.15$). These
 415 differences reflect the different types of boundary layers (i.e., $v(x)$, $w(x)$, and $W(x)$ in
 416 Fig. 1). (2) When wall plumes are parameterized, the entrainment coefficient α should
 417 use a much smaller value: $\alpha = 0.075$ for discharge plumes and $\alpha = 0.068$ for melt plumes.
 418 (3) Horizontal boundary layers $v(x)$ and their melt contribution should still be treated
 419 with the usual shear boundary layer width scales consistent with $C_d^{\text{ext}} = 2.5 \times 10^{-3}$.
 420 However, it is important to include the effect of this melt within the ambient melt plumes
 421 as their dynamics are sensitive to horizontal melt rates.

422 Currently, buoyancy fluxes and glacial melt rates at vertical ice-ocean interfaces
 423 are commonly parameterized using theories for unbounded free plumes and assume a uni-
 424 versal drag coefficient. However, both Direct Numerical Simulations and laboratory ex-
 425 periments suggest that wall-bounded plumes leads to different plume entrainment and
 426 vertical velocity profiles (with differences between subglacial discharge and melt plumes)
 427 due to the presence of a shear boundary layer. In addition, a recently data-supported
 428 parameterization of the turbulent transfer function that merges the velocity-dependent
 429 and -independent (buoyancy-dominated) melt regimes (Schulz et al., 2022) found a sig-
 430 nificantly higher baseline buoyancy-dominated melt rate than previous literature (e.g.,
 431 Kerr and McConnochie (2015)). Our study reconciles these inconsistencies using a physically-
 432 motivated melt parameterization that includes both convective- and shear-dominated
 433 melt regimes and is broadly consistent with existing observations, laboratory experiments,
 434 and field data.

435 We compare the predictions of free plume and wall-bounded plume theories to a
 436 discharge plume-resolving LES (MITgcm). We show that these LES results are consis-
 437 tent with previous theories for the along-plume and across-plume profiles of vertical mo-
 438 mentum. Finally, we demonstrate that using the wall-bounded plume modifications leads
 439 to a 40x factor increase in melt rate prediction for LeConte Glacier, which is necessary
 440 for consistency with existing observations.

441 Future work may test these parameterizations for consistency with other direct ob-
 442 servations near vertical ice faces including warm and cold glaciers and icebergs. Addi-
 443 tional modeling studies at both the LES and DNS resolution are needed to understand
 444 melt plumes, especially for transitions from buoyancy-dominated to shear-dominated bound-

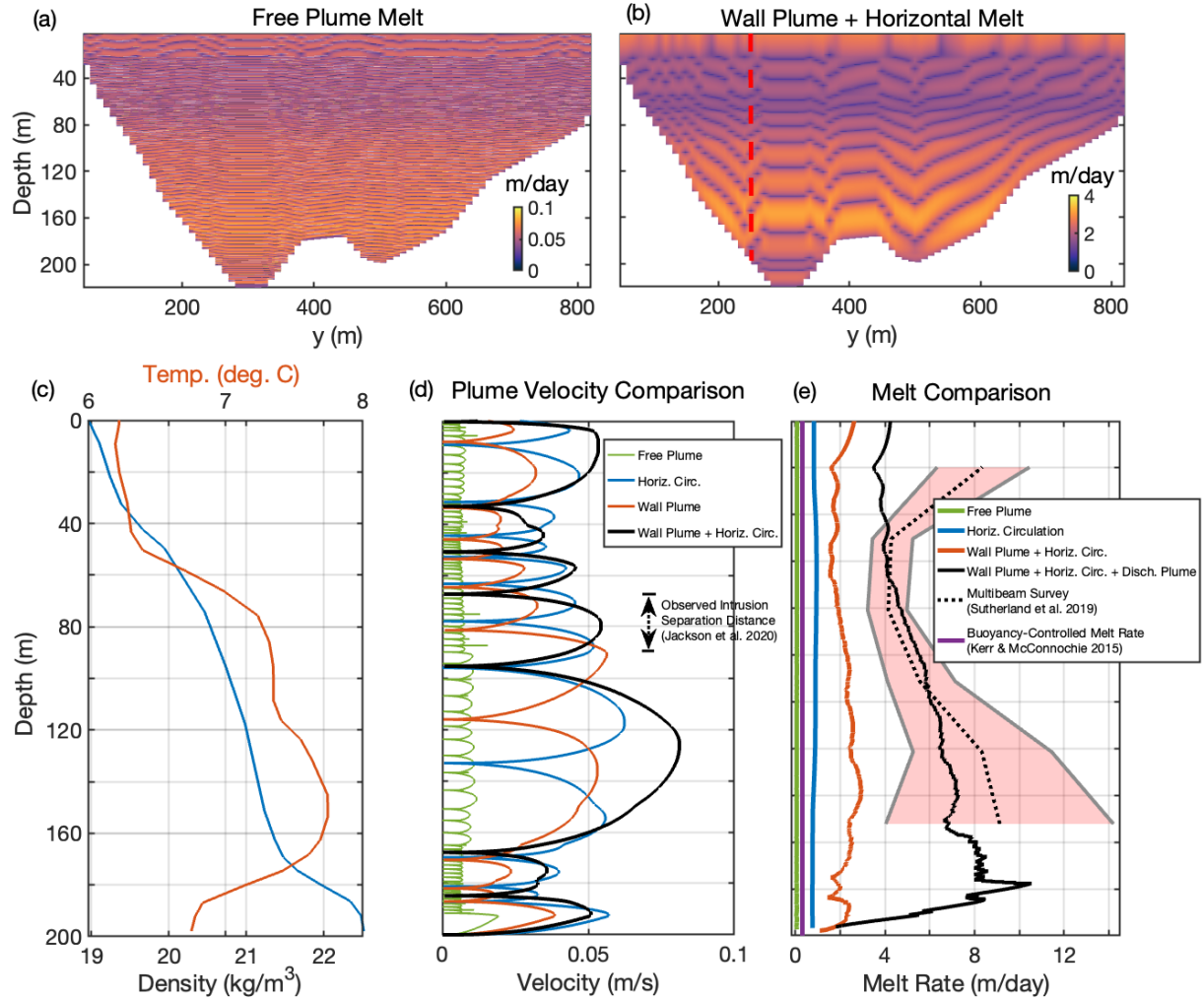


Figure 4. Melt rates at the LeConte glacier face calculated using (a) free plume parameters (Jackson et al., 2019), and (b) wall plume parameters with an additional horizontal circulation melt contribution driven by a uniform horizontal velocity of $v = 0.2$ m/s. Note that the color ranges between panels (a) and (b) differ by a factor of 40. (c) Temperature and salinity profiles from Sutherland et al. (2019) used in the calculations. (d) The plume velocity as a function of depth (assuming a starting depth of 200 m, as in the location dotted red line in panel b) for free plume parameters (green), a free plume with horizontal circulation (blue), wall plume parameters (red), and wall plume parameters with horizontal velocity (black). The observed mid-depth intrusion separation of approx. 20 m in Jackson et al. (2019) is shown for comparison. (e) The meridionally-averaged melt rate for various theories and approximations is shown and compared to the repeat multibeam survey-based estimates from Sutherland et al. (2019). In addition to the cases considered in (d), an additional line discharge plume (with total discharge rate of $220 \text{ m}^3/\text{s}$ imposed between $y = 250$ m and 350 m) and a buoyancy-controlled boundary layer melt estimate (Kerr & McConnochie, 2015) are shown for comparison.

445 ary layers and in the presence of both plumes and external velocity forcing. In addition,
 446 we may extend these ideas to sloping and geometrically-complex ice-ocean interfaces in-
 447 cluding ice-shelf cavity geometries, which may also included transition region from near-
 448 vertical interfaces to near-horizontal interfaces. Finally, direct observations of the entrain-
 449 ment rate, melt rate, and the boundary layer profiles of both discharge and melt plumes
 450 are necessary to improve our understanding of ice-ocean boundaries.

451 Acknowledgments

452 The authors would like to thank Dave Sutherland for assistance with the LeConte
 453 multibeam data, which is available at: <https://doi.org/10.18739/A22G44>. This mate-
 454 rial is based in part upon work supported by the National Science Foundation Office of
 455 Polar Programs Postdoctoral Fellowship under Grant OPP-2138790, and OPP-2023674.
 456 This work used computational resources supported by the NASA FINESST Fellowship
 457 under Grant 80NSSC20K163. The MITgcm model configuration and test case is avail-
 458 able at: https://github.com/zhazorken/MITgcm_FJ.

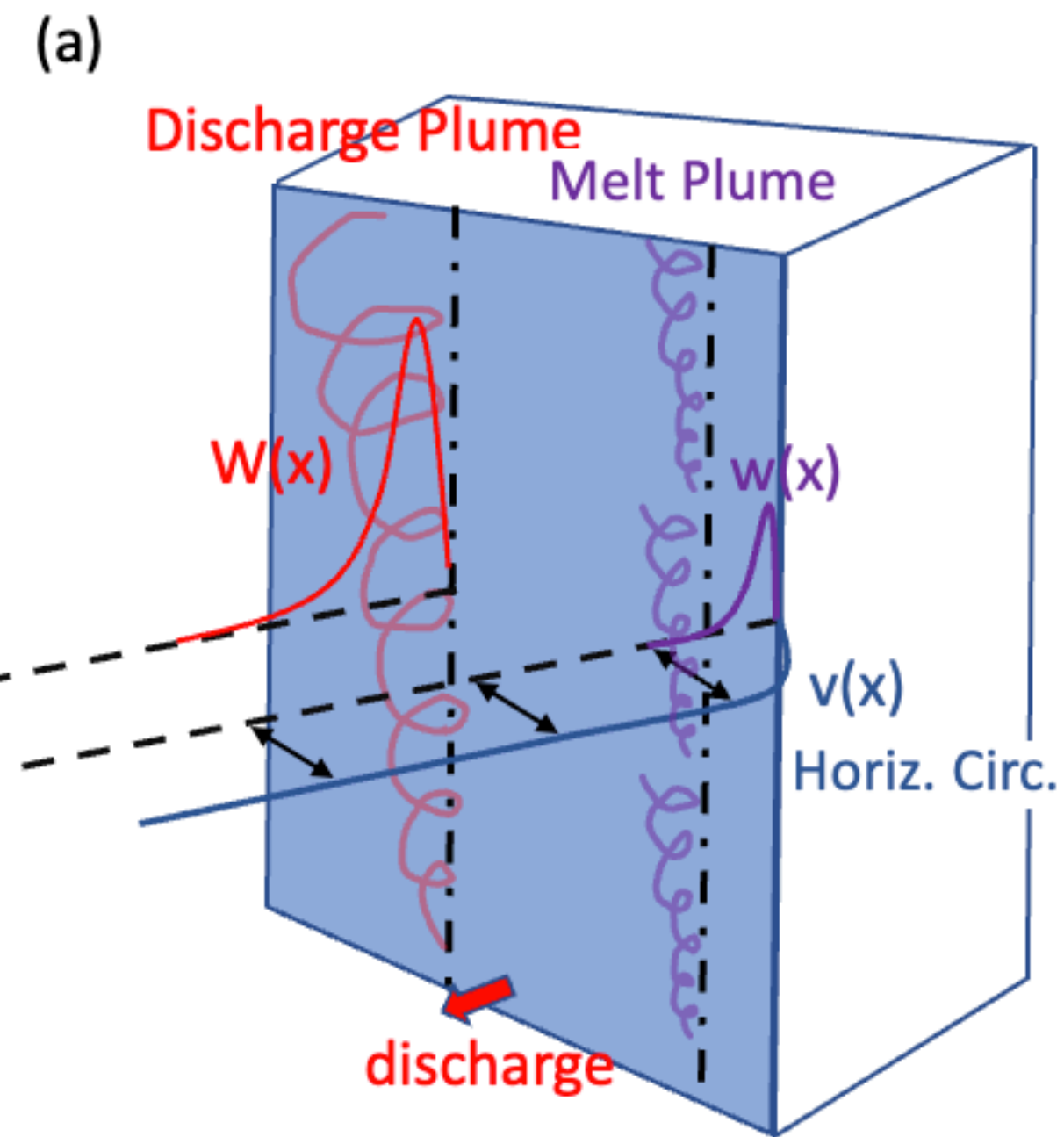
459 References

- 460 Carroll, D., Sutherland, D. A., Hudson, B., Moon, T., Catania, G. A., Shroyer,
 461 E. L., ... van den Broeke, M. R. (2016). The impact of glacier geometry on
 462 meltwater plume structure and submarine melt in greenland fjords. *Geophys.*
 463 *Res. Lett.*, *43*(18), 9739–9748. doi: 10.1002/2016GL070170
- 464 Cowton, T., Slater, D., Sole, A., Goldberg, D., & Nienow, P. (2015). Modeling the
 465 impact of glacial runoff on fjord circulation and submarine melt rate using
 466 a new subgrid-scale parameterization for glacial plumes. *J. Geophys. Res.*
 467 *Oceans*, *120*, 796–812.
- 468 Cowton, T., Sole, A. J., Nienow, P. W., Slater, D. A., & Christoffersen, P. (2018).
 469 Linear response of east greenland’s tidewater glaciers to ocean/atmosphere
 470 warming. *Proc. Natl. Acad. Sci. (USA)*, *115*(31), 7907–7912. doi:
 471 10.1073/pnas.1801769115
- 472 Eckert, E., & Jackson, T. (1950). *Analysis of Turbulent Free-Convection Boundary*
 473 *Layer on Flat Plate*. Washington.
- 474 Fried, M. J., Catania, G. A., Bartholomaeus, T. C., Duncan, D., Davis, M., Stearns,
 475 L. A., ... Sutherland, D. (2015). Distributed subglacial discharge drives sig-
 476 nificant submarine melt at a greenland tidewater glacier. *Geophys. Res. Lett.*,
 477 *42*(21), 9328–9336. doi: 10.1002/2015GL065806
- 478 Gayen, B., Griffiths, R. W., & Kerr, R. C. (2016). Simulation of convection at a ver-
 479 tical ice face dissolving into saline water. *J. Fluid Mech.*, *798*, 284–298.
- 480 Grossmann, S., & Lohse, D. (2000). Scaling in thermal convection: a unifying the-
 481 ory. *J. Fluid Mech.*, *407*, 27–56.
- 482 Hewitt, I. (2020). Subglacial Plumes. *Annu. Rev. Fluid Mech.*, *52*, 145–169. doi:
 483 annurev-fluid-010719-060252
- 484 Holland, P. R., Jenkins, A., & Holland, D. M. (2008). The response of ice shelf basal
 485 melting to variations in ocean temperature. *J. Climate*, *21*, 2258–2272. doi: 10
 486 .1175/2007JCLI1909.1
- 487 Jackson, R. H., Nash, J. D., Kienholz, C., Sutherland, D. A., Amundson, J. M.,
 488 Motyka, R. J., ... Pettit, E. (2019). Meltwater intrusions reveal mechanisms
 489 for rapid submarine melt at a tidewater glacier. *Geophys. Res. Lett.* doi:
 490 10.1029/2019GL085335
- 491 Jackson, R. H., Shroyer, E. L., Nash, J. D., Sutherland, D. A., Carroll, D., Fried,
 492 M. J., ... Stearns, L. A. (2017). Near-glacier surveying of a subglacial dis-
 493 charge plume: Implications for plume parameterizations. *Geophys. Res. Lett.*,
 494 *44*(13), 6886–6894. doi: 10.1002/2017GL073602

- 495 Jenkins, A. (1991). A one-dimensional model of ice shelf-ocean interaction. *J. Geophys. Res. Oceans*, *96*, 20671–20677.
- 496
- 497 Jenkins, A. (2011). Convection-Driven Melting near the Grounding Lines of Ice
498 Shelves and Tidewater Glaciers. *J. Phys. Oceanogr.*, *41*(12), 2279–2294. doi: 10
499 .1175/JPO-D-11-03.1
- 500 Jenkins, A., Dutrieux, P., Jacobs, S., McPhail, S., Perrett, J., Webb, A., & White,
501 D. (2010). Observations beneath Pine Island Glacier in West Antarctica and
502 implications for its retreat. *Nat. Geosci.*, *3*, 468–472.
- 503 Josberger, E. G., & Martin, S. (1981). A laboratory and theoretical study of the
504 boundary layer adjacent to a vertical melting ice wall in salt water. *J. Fluid
505 Mech.*, *111*, 439–473. doi: 10.1017/S0022112081002450
- 506 Kaimal, J. C., & Finnigan, J. J. (1994). *Atmospheric Boundary Layer Flows:
507 Their Structure and Measurement*. Oxford University Press. Retrieved
508 from <https://doi.org/10.1093/oso/9780195062397.001.0001> doi:
509 10.1093/oso/9780195062397.001.0001
- 510 Kerr, R. C., & McConnochie, C. D. (2015). Dissolution of a vertical solid surface by
511 turbulent compositional convection. *J. Fluid Mech.*, *765*, 211–228. doi: doi:10
512 .1017/jfm.2014.722
- 513 Malyarenko, A., Wells, A. J., Langhorne, P. J., Robinson, N. J., Williams, M. J., &
514 Nicholls, K. W. (2020). A synthesis of thermodynamic ablation at ice–ocean
515 interfaces from theory, observations and models. *Ocean Modelling*, *154*,
516 101692. doi: <https://doi.org/10.1016/j.ocemod.2020.101692>
- 517 Marshall, J. A., Hill, C., Perelman, L., & Heisey, C. (1997). A finite-volume, incom-
518 pressible navier stokes model for studies of the ocean on parallel computers. *J.
519 Geophys. Res.*, *102* (C3), 5753–5766.
- 520 McConnochie, C. D., & Kerr, R. C. (2017a). Enhanced ablation of a vertical ice wall
521 due to an external freshwater plume. *J. Fluid Mech.*, *810*, 429–447. doi: doi:10
522 .1017/jfm.2016.761
- 523 McConnochie, C. D., & Kerr, R. C. (2017b). Testing a common ice-ocean parame-
524 terization with laboratory experiments. *J. Geophys. Res.*, *122*, 5905–5915. doi:
525 doi:10.1002/2017JC012918
- 526 McPhee, M. G., Morison, J. H., & Maykut, G. A. (1987). Dynamics and ther-
527 modynamics of the ice/upper ocean system in the marginal ice zone of the
528 Greenland Sea. *J. Geophys. Res.*, *92*, 7017–7031.
- 529 McPhee, M. G., Morison, J. H., & Nilsen, F. (2008). Revisiting heat and salt ex-
530 change at the ice-ocean interface: Ocean flux and modeling considerations. *J.
531 Geophys. Res.*, *113*, C06014. doi: 10.1029/2007JC004383
- 532 Morton, B. R., Taylor, G. I., & Turner, J. S. (1956). Turbulent gravitational con-
533 vection from maintained and instantaneous sources. *Proceedings of the Royal
534 Society of London. Series A. Mathematical and Physical Sciences*, *234* (1196),
535 1–23. doi: 10.1098/rspa.1956.0011
- 536 Paillat, S., & Kaminski, E. (2014). Entrainment in plane turbulent pure plumes. *J.
537 Fluid Mech.*, *755*, R2.
- 538 Parker, D. A., Burridge, H. C., Partridge, J. L., & Linden, P. F. (2020). A com-
539 parison of entrainment in turbulent line plumes adjacent to and distant from a
540 vertical wall. *J. Fluid Mech.*, *882*, A4. doi: doi:10.1017/jfm.2019.790
- 541 Parker, D. A., Burridge, H. C., Partridge, J. L., & Linden, P. F. (2021). Vertically
542 distributed wall sources of buoyancy. Part 1. Unconfined. *J. Fluid Mech.*, *907*,
543 A15. doi: doi:10.1017/jfm.2020.808
- 544 Pope, S. B. (2000). *Turbulent flows*. Cambridge University Press. doi: 10.1017/
545 CBO9780511840531
- 546 Ramaprian, M. S., B. R. Chandrasekhara. (1989). Measurements in vertical plane
547 turbulent plumes. *Trans. ASME J. Fluids Engng.*, *111*, 69–77.
- 548 Sangras, R., Dai, Z., & Faeth, G. M. (2000). Velocity statistics of plane self-
549 preserving buoyant turbulent adiabatic wall plumes. *Trans. ASME J. Heat*

- 550 *Transfer*, 122 (4), 693–700.
- 551 Schulz, K., Nguyen, A. T., & Pillar, H. R. (2022). An Improved and
552 Observationally-Constrained Melt Rate Parameterization for Vertical Ice
553 Fronts of Marine Terminating Glaciers. *Geophys. Res. Lett.*, 49(18),
554 e2022GL100654. doi: <https://doi.org/10.1029/2022GL100654>
- 555 Slater, D. A., Straneo, F., Das, S. B., Richards, C. G., Wagner, T. J. W., & Nienow,
556 P. W. (2018). Localized Plumes Drive Front-Wide Ocean Melting of A Green-
557 landic Tidewater Glacier. *Geophys. Res. Lett.*, 45(22), 12,350 – 12,358. doi:
558 10.1029/2018GL080763
- 559 Smagorinsky, J. (1963). General circulation experiments with the primitive equa-
560 tions: I. the basic experiment. *Mon. Wea. Rev.*, 91(3), 99 - 164. doi: [https://doi.org/10.1175/1520-0493\(1963\)091<0099:GCEWTP>2.3.CO;2](https://doi.org/10.1175/1520-0493(1963)091<0099:GCEWTP>2.3.CO;2)
- 561 Straneo, F., & Cenedese, C. (2015). The Dynamics of Greenland’s Glacial Fjords
562 and Their Role in Climate. *Annu. Rev. Mar. Sci.*, 7(1), 89-112. doi: 10.1146/
563 annurev-marine-010213-135133
- 564 Straneo, F., & Heimbach, P. (2013). North Atlantic Warming and the Retreat of
565 Greenland’s Outlet Glaciers. *Nature*, 504(7478), 36–43. doi: <https://doi.org/10.1038/nature12854>
- 566 Sutherland, D. A., Jackson, R. H., Kienholz, C., Amundson, J. M., Dryer, W. P.,
567 Duncan, D., ... Nash, J. D. (2019). Direct observations of submarine melt and
568 subsurface geometry at a tidewater glacier. *Science*, 365(6451), 369–374. doi:
569 10.1126/science.aax3528
- 570 Sutherland, D. A., Straneo, F., & Pickart, R. S. (2014). Characteristics and dynam-
571 ics of two major Greenland glacial fjords. *J. Geophys. Res. Oceans*, 119(6),
572 3767-3791. doi: 10.1002/2013JC009786
- 573 Turner, J. S. (1979). *Buoyancy effects in fluids*. Cambridge University Press Paper-
574 back.
- 575 van den Broeke, M. R., Enderlin, E. M., Howat, I. M., Munneke, P. K., Noël,
576 B. P. Y., van de Berg, W. J., ... Wouters, B. (2016). On the recent con-
577 tribution of the Greenland ice sheet to sea level change. *The Cryosphere*, 10,
578 1933–1946. doi: 10.5194/tc-10-1933-2016
- 579 Vreugdenhil, C. A., & Taylor, J. R. (2019). Stratification effects in the turbulent
580 boundary layer beneath a melting ice shelf: Insights from resolved large-eddy
581 simulations. *Journal of Physical Oceanography*, 49(7), 1905 - 1925. Re-
582 trieved from [https://journals.ametsoc.org/view/journals/phoc/49/7/](https://journals.ametsoc.org/view/journals/phoc/49/7/jpo-d-18-0252.1.xml)
583 [jpo-d-18-0252.1.xml](https://journals.ametsoc.org/view/journals/phoc/49/7/jpo-d-18-0252.1.xml) doi: <https://doi.org/10.1175/JPO-D-18-0252.1>
- 584 Wells, A., & Worster, M. (2008). A geophysical-scale model of vertical natural con-
585 vection boundary layers. , 609, 111–137. doi: 10.1017/S0022112008002346
- 586 Wood, M., Rignot, E., Fenty, I., Menemenlis, D., Millan, R., Morlighem, M.,
587 ... Seroussi, H. (2018). Ocean-Induced Melt Triggers Glacier Retreat
588 in Northwest Greenland. *Geophys. Res. Lett.*, 45(16), 8334–8342. doi:
589 10.1029/2018GL078024
- 590 Zhao, K. X., Stewart, A. L., & McWilliams, J. C. (2021). Geometric Constraints on
591 Glacial Fjord–Shelf Exchange. *J. Phys. Oceanogr.*, 51 (4), 1223–1246. doi: 10
592 .1175/JPO-D-20-0091.1
- 593 Zhao, K. X., Stewart, A. L., & McWilliams, J. C. (2022). Linking Overturn-
594 ing, Recirculation, and Melt in Glacial Fjords. *Geophys. Res. Lett.*, 49(15),
595 e2021GL095706. doi: <https://doi.org/10.1029/2021GL095706>
- 596 Zhao, K. X., Stewart, A. L., McWilliams, J. C., Fenty, I. G., & Rignot, E. J.
597 (2023). Standing eddies in glacial fjords and their role in fjord circula-
598 tion and melt. *Journal of Physical Oceanography*, 53(3), 821 - 840. doi:
599 <https://doi.org/10.1175/JPO-D-22-0085.1>

Figure 1.



(b)	Drag Coefficient (C_d)	Entrainment (α)	References
Discharge Wall Plume	0.012 - 0.018	0.065 - 0.085	Parker et al. 2021, Greela et al. 1975, Lai et al. 1987, Sangras et al. 2000
Melt Wall Plume	0.12 - 0.18	0.06 - 0.079	Parker et al. 2021, Gayen et al. 2016, Kerr et al. 2015, Cheesewright 1968
Horizontal Circulation	0.0025	-	McPhee et al. 1987, Jenkins 2011, many others
Free Plume (Line)	0.0025	0.10 - 0.13	Jenkins 2011, Cowton et al. 2015, many others

Figure 2.

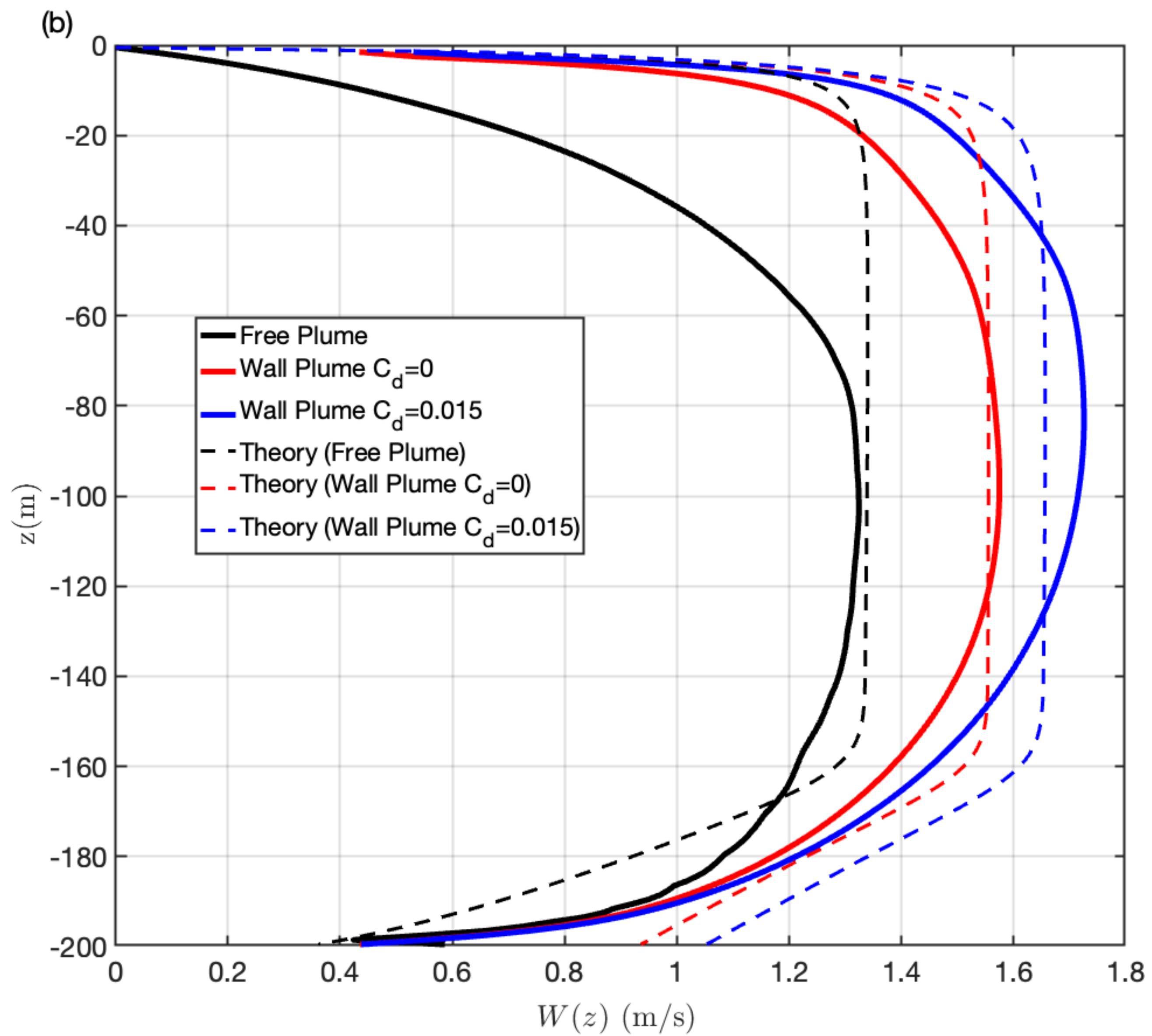
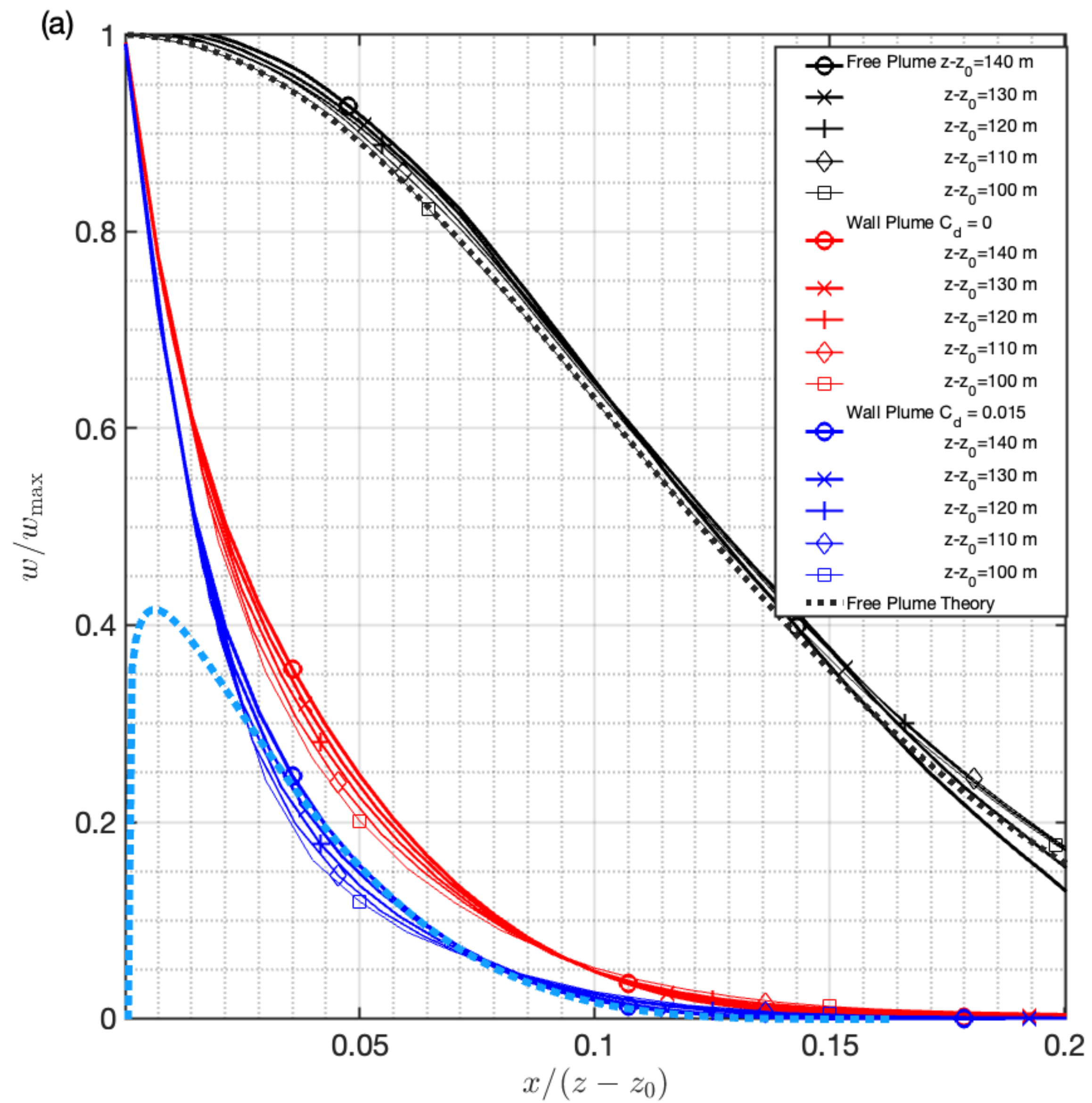


Figure 3.

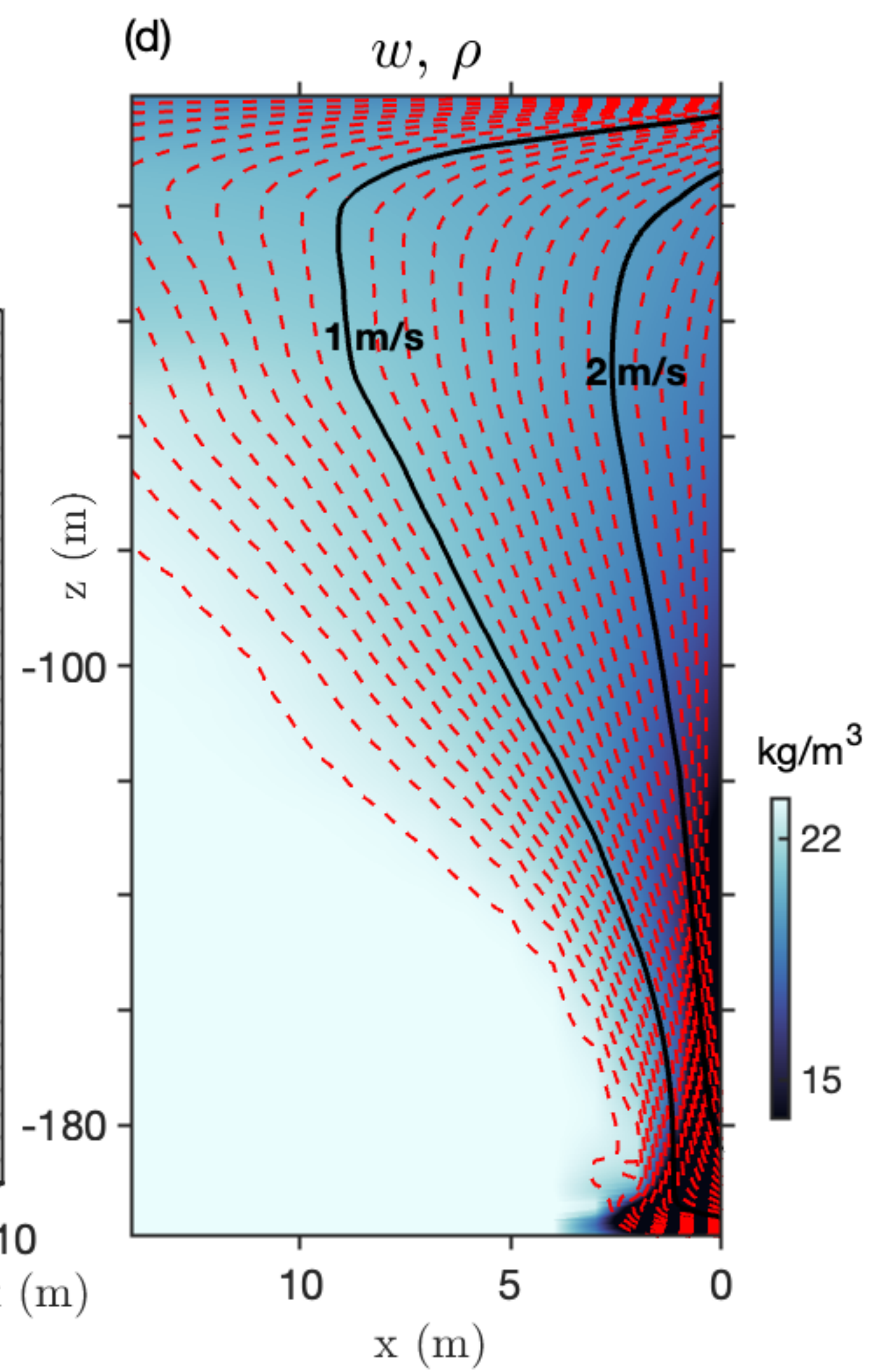
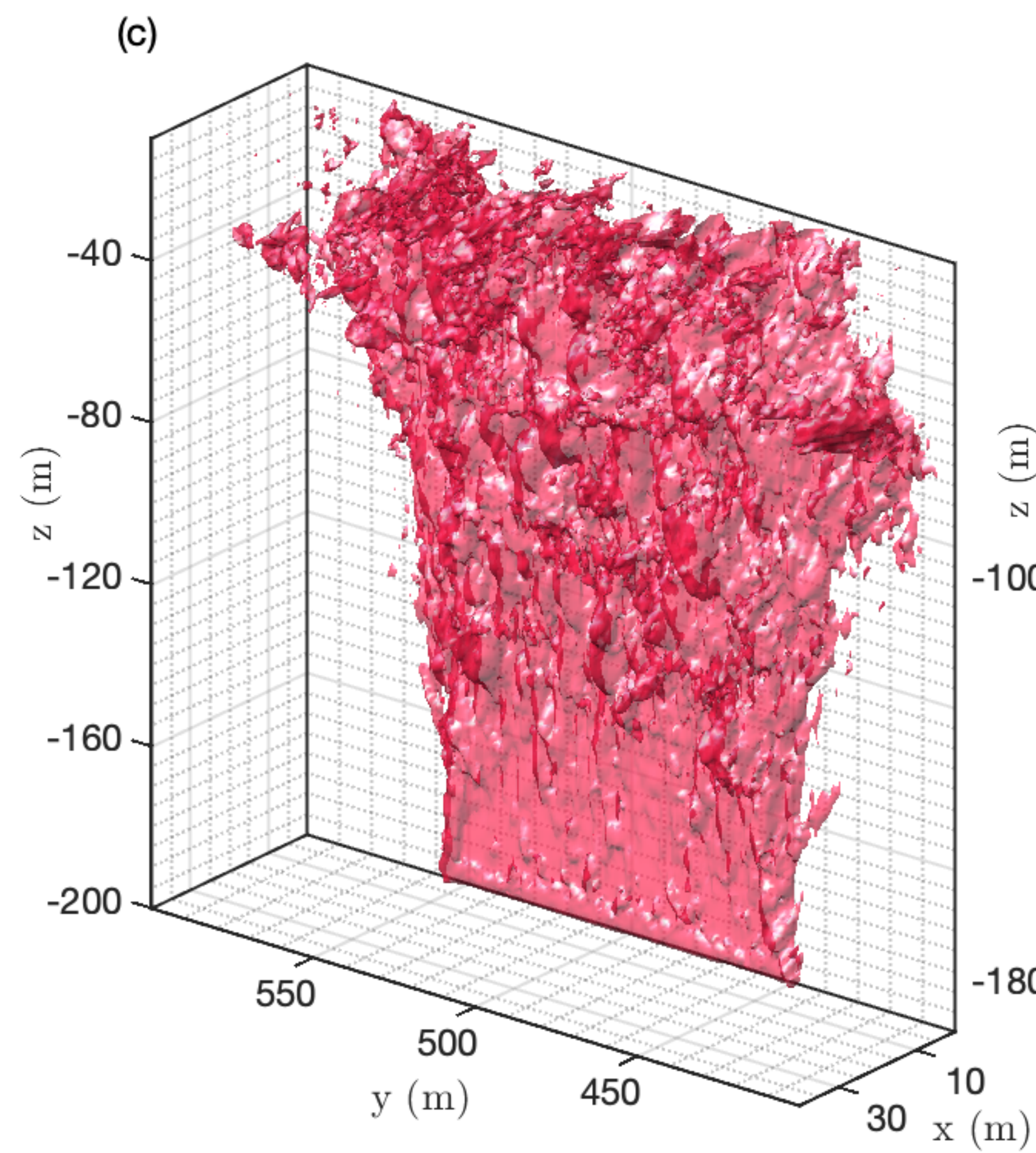
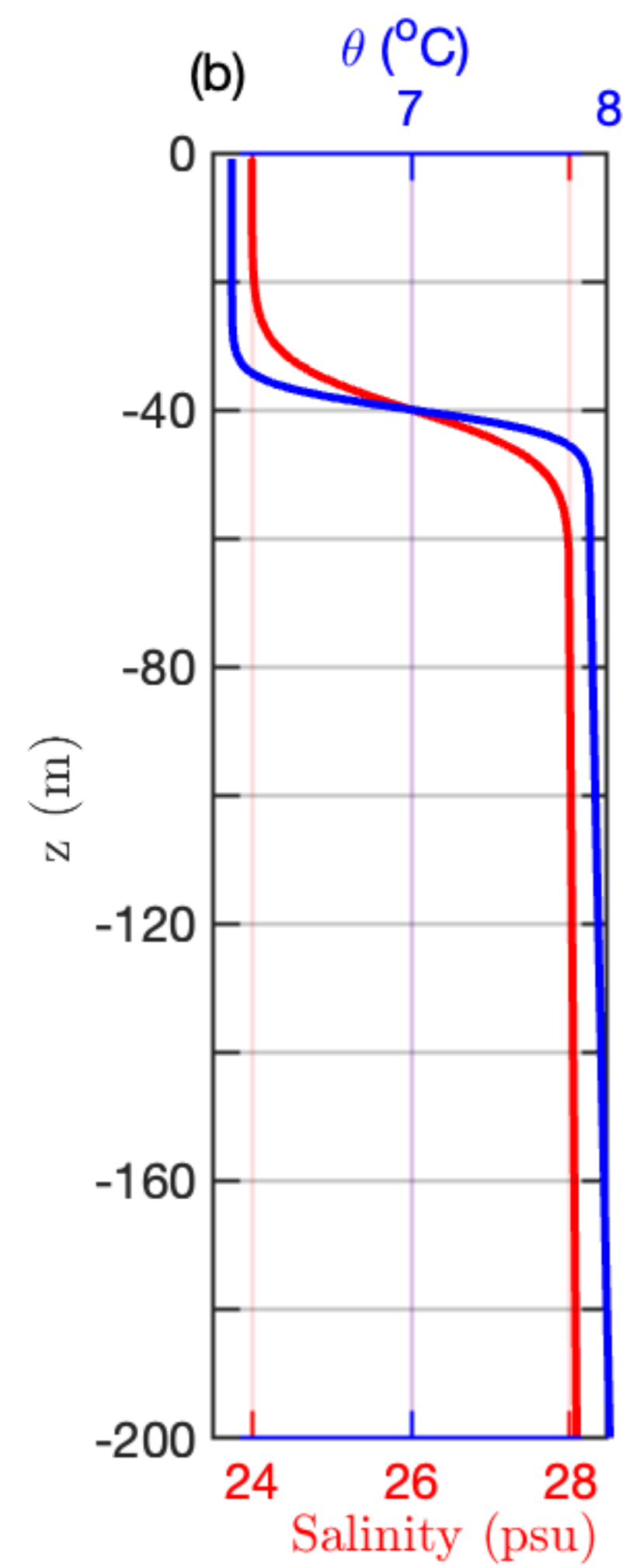
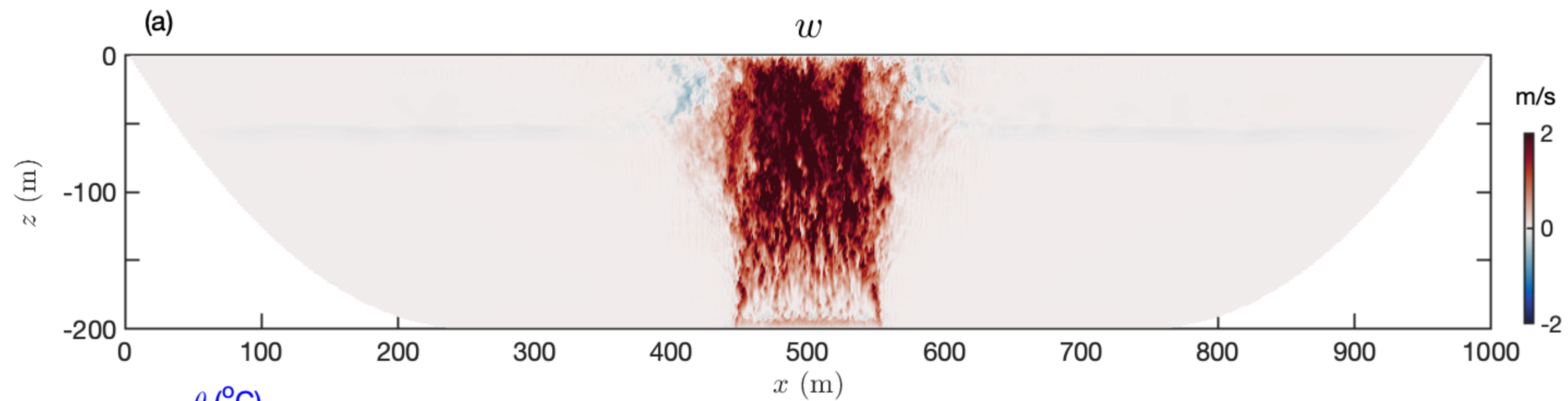


Figure 4.

